PASJ: Publ. Astron. Soc. Japan **48**, 305–315 (1996)

Emission-Line Profiles from Be-Star Envelopes with $m = 1$ Perturbation Patterns

Atsuo T. OKAZAKI *
Astronomical Institute 'Anton Pannekoek', University of Amsterdam, Kruislaan 403, 1098 SJ Amsterdam, The Netherlands.

(Received 1991 January 30; accepted 1996 January 25)

Abstract

We have studied the variations in the Balmer-line profiles from Be-star disks with eccentric (i.e., $m = 1$) perturbation patterns. In order to examine the effects of oscillations on the line profiles, we assumed that the nonlinear perturbation patterns are similar to the linear $m = 1$ eigenfunctions. In addition, we assumed that the source function is constant over the entire disk. Based on these assumptions, we computed the optically-thick line profiles for various values of the disk parameters. We found that the line-profile variability due to the $m = 1$ perturbation patterns agrees well with the observed V/R variability. We also found that the amplitude of the profile shift associated with the V/R variation is sensitive to the density gradient in the radial direction. In particular, disks in which the local density decreases as steeply as r^{-3} exhibit remarkable variabilities like the observed V/R variations. These variabilities occur for a wide range of disk sizes and line optical depths.

Key words: Line profiles — Stars: Be — Stars: circumstellar shells — Stars: emission lines — Stars: variable

-

1. Introduction

The long-term V/R variation is one of the most puzzling phenomena concerning Be stars. The periods of the variations range from years to decades; the average period is about 7 yr (Copeland, Heard 1963; Hirata, Hubert-Delplace 1981). This period range is much longer than the rotation periods of the central stars and cool envelopes. In addition, the variations are always accompanied by profile shifts: the profile as a whole shifts blueward (redward) when the red (violet) component is stronger (McLaughlin 1961, 1962, 1963, 1966; Hubert et al. 1987). A schematic picture of the profile variation is given by Huang (1975).

Because of their bizarreness, the long-term V/R variations have been extensively studied. Unfortunately, no widely-accepted models exist yet. However, it is now accepted that this phenomenon can be attributed to variations in cool envelopes surrounding the stars (e.g., Poeckert 1982; Hirata, Kogure 1984; Ballereau, Chauville 1989). Thus, any satisfactory model for the long-term V/R variations enables us to probe the disk structures and distributions of physical quantities in equatorial disks.

In Okazaki (1991, hereafter Paper I) we proposed a dynamical model based on a theory of global oscillations in nonself-gravitating, geometrically thin (i.e., nearly Keplerian) disks. According to this theory of global oscillations, the possible global oscillations in nearly Keplerian disks are very low-frequency, one-armed (i.e., $m = 1$) oscillations alone (Kato 1983, 1989; Okazaki, Kato 1985; Adams et al. 1989; Okazaki 1991). Hence, this model suggests that the long-term V/R variations are phenomena caused by the global $m = 1$ oscillations in the equatorial disks of Be stars. Studying the $m = 1$ eigenmodes of linear isothermal oscillations in the isothermal equatorial disks, we found in Paper I that the one-armed oscillation model naturally explains the observed periodicities of the long-term V/R variations.

Recently, based on 3D radiative-transfer calculations, Hummel and Hanuschik (1994) and Hanuschik et al. (1995) presented some examples of the Hα emission line profiles from disks with the perturbation patterns found in Paper I. They found that the computed profiles are in agreement with the observed line-profile variability.

The purpose of this paper is to discuss our examination of the behavior of the line-profile variations due to the $m = 1$ perturbation patterns for various values of

* On leave from College of General Education, Hokkai-Gakuen University, Toyohira-ku, Sapporo 062, Japan.

the disk parameters. Since we were concerned with the global features of V/R variations, we adopted a simplified treatment, which is described in later sections. We computed the line profiles by integrating the fluxes along the line-of-sights through the entire disk region. Similar methods have often been used to calculate the profiles of optically-thick lines emitted from disks (e.g., Marlborough 1969, 1970; Poeckert, Marlborough 1978 for Be-star envelopes, and Horne, Marsh 1986; Adam et al. 1989a,b for accretion disks).

In this paper we show that, in general terms, the line-profile variabilities caused by the $m=1$ perturbation patterns are in agreement with the observed V/R variations. We also show that the amplitude of the profile shift associated with the V/R variation is sensitive to the adopted detailed disk structure. In the model described, disks with a local density which decreases as steeply as r^{-3} exhibit remarkable V/R variations for a wide range of disk parameters.

2. $m = 1$ Perturbation Patterns in Isothermal Equatorial Disks

In Paper I we decribed in detail the basic disk model and properties of the $m=1$ eigenmodes in equatorial disks of Be stars. The disk model adopted in this paper is the same as that adopted in Paper I, except that the present model includes the quadrupole contribution to the potential of a rotationally distorted central star, according to Papaloizou et al. (1992) and Savonije and Heemskerk (1993). As shown below, however, including the quadrupole contribution to the potential does not affect the eigenmodes qualitatively. Hence, in this section we give only a brief summary of the unperturbed disk model and the $m=1$ perturbation patterns.

2.1. The Unperturbed Disk Model

We assume that an unperturbed disk is steady, axisymmetric, and nearly Keplerian. For simplicity, the disk was assumed to be isothermal; the disk temperature adopted was 2/3 of the effective temperature of the central star. In addition, we assumed that the disk extends from the surface of the central star ($r=r_\mathrm{s}$) to the outer radius ($r=r_\mathrm{out}$). The adopted value of the mean molecular weight was 0.6. We took a B0 main-sequence star as being a typical central star, because many Be stars exhibiting long-term V/R variations are early B stars (Hirata, Hubert-Delplace 1981). The quantities characterizing the central star were from Allen (1973) (see table 1 of Paper I).

We used a cylindrical coordinate system (r,ϕ,z) to describe the disk; the origin is at the center of the star and the z-axis is perpendicular to the disk midplane. For convenience's sake, we assume in later sections that the projection of the observer's direction onto the equatorial plane is at $\phi=0$.

From the equation describing the hydrostatic balance of the disk in the vertical direction, we obtain the density distribution in the vertical direction,

$$\rho_0\,(r,z)=\rho_{00}(r)\exp\left(-\frac{z^2}{2H^2}\right), \tag{1}$$

where ρ_0 is the unperturbed density, ρ_{00} is the unperturbed density on the equatorial plane, and H is the vertical scale-height of the disk, given by

$$H(r)=\frac{c_\mathrm{s}}{\Omega_\mathrm{K}(r)}\propto\left(\frac{r}{r_\mathrm{s}}\right)^{3/2}. \tag{2}$$

Here, c_s and Ω_K are the isothermal sound speed and the Keplerian angular frequency, respectively.

At present, the density profiles of the Be-star disks are not well determined observationally. Hence, we adopt a simple power-law form for ρ_{00},

$$\rho_{00}\,(r)\propto\left(\frac{r}{r_\mathrm{s}}\right)^{-\alpha}, \tag{3}$$

where the index α is a constant. The surface density is then proportional to $r^{\frac{3}{2}-\alpha}$.

In the present model, the angular frequency of disk rotation Ω and the epicyclic frequency κ are written in the form

$$\Omega(r)=\Omega_\mathrm{K}(r)\left[1-\alpha\left(\frac{H}{r}\right)^2+k_2f^2\left(\frac{r}{r_\mathrm{s}}\right)^{-2}\right]^{1/2} \tag{4}$$

and

$$\kappa(r)=\Omega_\mathrm{K}(r)\left[1-2\alpha\left(\frac{H}{r}\right)^2-k_2f^2\left(\frac{r}{r_\mathrm{s}}\right)^{-2}\right]^{1/2}. \tag{5}$$

Here, k_2 is the apsidal motion constant and f is a measure of the central star's rotation rate, defined by

$$f=\frac{\Omega_\mathrm{s}}{\Omega_\mathrm{K}(r_\mathrm{s})}, \tag{6}$$

where Ω_s is the angular frequency of the central star (Papaloizou et al. 1992; Savonije, Heemskerk 1993). Note that the second and third terms in each square brackets in equations (4) and (5) denote the contribution due to the pressure-gradient force in the disk and the quadrupole contribution to the potential of the rotationally distorted central star, respectively.

In the remainder of this subsection we discuss the effect of the rotational deformation of the central star. Papaloizou et al. (1992) and Savonije and Heemskerk (1993) claimed that $m=1$ oscillations are confined to the inner part of Be-star disks by including the quadrupole contribution to the potential of a rotationally distorted central star. In Okazaki (1991), since the $m = 1$ oscillations were not confined naturally, truncation of the disk was assumed. We show in the following paragraphs that the above conclusions obtained by Papaloizou et al. (1992) and Savonije and Heemskerk (1993) do not generally hold for Be-star disks. For Be stars, the effect of the rotational deformation of the central star is comparable even in the innermost region of the disk, and decreases rapidly with increasing r.

Papaloizou et al. (1992) adopted $(H/r)^2 \sim 10^{-4}$, which corresponds to the disk temperature, $T_{\rm disk} \sim 3300(r/r_{\rm s})^{-1}$K, for a B0-type star and $T_{\rm disk} \sim 2300(r/r_{\rm s})^{-1}$K for a B5-type star. This temperature is too low as a model for the Be-star disks. Savonije and Heemskerk (1993) studied $m = 1$ oscillations in disks with $10^{-4} \leq (H/r)^2 \leq 4\times10^{-4}$ and $2\times10^{-3} \leq k_2 f^2 \leq 10^{-2}$ around a star of $M = 8M_{\odot}$ and $r_{\rm s} = 5R_{\odot}$. These parameter ranges cover $2200(r/r_{\rm s})^{-1}{\rm K} \leq T_{\rm disk} \leq 8900(r/r_{\rm s})^{-1}$K and $0.58\,(k_2/6\times10^{-3})^{-1/2} \leq \Omega_{\rm s}/\Omega_{\rm K}(r_{\rm s}) \leq 1.3\,(k_2/6\times10^{-3})^{-1/2}$. Here, we normalized k_2 using the value adopted in Papaloizou et al. (1992). The value of k_2 strongly depends on the internal structure of the star, and is not determined well (Claret, Giménez 1991). If $k_2 \gtrsim 10^{-2}$, the above range of the stellar rotation rate covers that for actual Be stars. However, the temperature range in their study was still too low to apply to the Be-star disks.

We can evaluate the effects by the pressure force and the rotational deformation of the central star for the present disk model by studying the free-particle precession frequency,

$$\Omega - \kappa \sim \frac{1}{2}\Omega_{\rm K}(r)\,[\Delta_{\rm p}(r) + \Delta_{\rm d}(r)]\,. \tag{7}$$

Here, $\Delta_{\rm p}$ and $\Delta_{\rm d}$, the measures of these effects, are given by

$$\Delta_{\rm p}(r) = \alpha\left[\frac{H(r_{\rm s})}{r_{\rm s}}\right]^2\frac{r}{r_{\rm s}} \tag{8}$$

and

$$\Delta_{\rm d}(r) = 2k_2 f^2\left(\frac{r}{r_{\rm s}}\right)^{-2}. \tag{9}$$

For the present model, the ratio of these two quantities is

$$\frac{\Delta_{\rm d}}{\Delta_{\rm p}} \sim 3.4\alpha^{-1}\frac{k_2}{6\times10^{-3}}\left(\frac{f}{0.4}\right)^2\left(\frac{r}{r_{\rm s}}\right)^{-3}. \tag{10}$$

For B0-type Be stars, $f \sim 0.2$–0.6 (see figure 4 of Kogure, Hirata 1982). Consequently, the effect of the rotational deformation of the central star is comparable to the pressure effect, even in the innermost region of the disk. For $r \gg r_{\rm s}$, the former is much weaker than the latter. Thus, we conclude that since the effect of the rotational deformation of the central star is not generally important in the disks of Be stars, including this effect does not qualitatively change the results obtained by Okazaki (1991). It is important only for the cases $k_2 > 10^{-2}$ and $f \sim 1$.

2.2. $m = 1$ Perturbation Patterns

Using the method described in Paper I, we can solve the linearized equations for isothermal perturbations in the form of normal modes which vary as $\exp[i(\omega t - \phi)]$. As mentioned above, the eigenmodes obtained are qualitatively the same as those in Paper I. They naturally explain some of the observational features of the long-term V/R variations of Be stars. However, since these eigenmodes are linear, the model does not predict either the amplitude of the variation or the behavior of the profile shift. It is thus very important to study even qualitative effects of $m = 1$ oscillations on the line profiles.

For this purpose, we assume that the nonlinear perturbation patterns are similar to the linear eigenfunctions. We normalize the amplitude of the perturbation so that the maximum value of the perturbed part of the angular velocity is 10 % of the unperturbed part. This value is adopted for clearly illustrating the effects of $m = 1$ perturbations on the line profiles. Based on this assumption, we investigate in later sections whether $m = 1$ perturbation patterns cause V/R variations similar to the observed variations of the Balmer lines.

Figure 1 shows the radial distributions of the relative amplitudes of some perturbed quantities associated with the fundamental modes for (a) $\alpha = 2$ and (b) $\alpha = 3$. The unperturbed disk extends up to $r_{\rm out}/r_{\rm s} = 10$. The solid, dotted, and dash-dotted curves denote ρ_1/ρ_0, $u_r/(r\Omega)$, and $u_\phi/(r\Omega)$, respectively. Here, ρ_1 is the Eulerian perturbation of the density and u_r and u_ϕ are the horizontal components of the velocity field associated with the perturbation. Note that ρ_1 and u_ϕ vary as $\cos(\omega t - \phi)$, while u_r varies as $\sin(\omega t - \phi)$. For each mode we present the oscillation period. The negative periods denote retrograde modes.

It is immediately observed that the density perturbation anticorrelates with the angular-velocity perturbation, except in the innermost $(r/r_{\rm s} \lesssim 2)$ region. Hence, we expect that the fundamental $m = 1$ mode shifts a double-peaked emission-line profile in the direction of the weaker emission component, unless the emission from the innermost region is dominant. Note that this profile shift is just one of the typical properties of the observed long-term V/R variations of Balmer lines.

3. Methods for Computing Emission Line Profiles

We consider only Balmer lines, which are assumed to be emitted from the entire disk. Neither the radiation from the central star nor the continuum radiation from

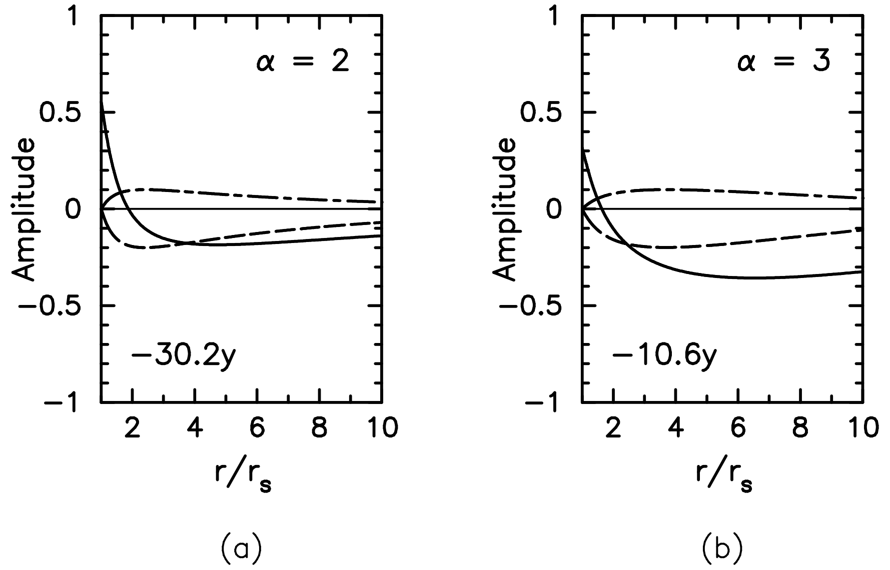

Fig. 1. Radial distribution of the relative amplitudes of perturbed quantities associated with the fundamental modes of one-armed isothermal oscillations for (a) $\alpha = 2$ and (b) $\alpha = 3$. The unperturbed disks extend to $r_{\rm out}/r_s = 10$. The solid, dotted, and dash-dotted curves denote ρ_1/ρ_0, $u_r/(r\Omega)$, and $u_\phi/(r\Omega)$, respectively. For each mode, the oscillation period is given. The negative periods denote retrograde modes.

the disk are included. In the Balmer-line regions of Be-star disks, hydrogen is almost fully ionized and electrons populate in accordance with an incomplete Rosseland cycle (i.e., the photoionization from the second energy level of hydrogen atoms followed by the recombination and the subsequent cascade transitions). Hence, we assume that the population density of the second energy level n is proportional to $(\rho_0 + \rho_1)^2$, i.e.,

$$n(r,\phi,z) \;=\; n_0(r,z)\left[1+\frac{\rho_{10}(r)}{\rho_{00}(r)}\cos(\omega t-\phi)\right]^2, \quad (11)$$

where ρ_{10} is the Eulerian perturbation of the density on the equatorial plane, and n_0 is the unperturbed population density, given by

$$n_0(r,z) \;=\; n_0(r_{\rm s},0)\left(\frac{r}{r_{\rm s}}\right)^{-2\alpha}\exp\left(-\frac{z^2}{H^2}\right). \quad (12)$$

We take into account only the thermal broadening as the line-broadening mechanism. The line-absorption coefficient κ_v at a line-of-sight velocity v is then expressed as

$$\kappa_v \;=\; \frac{\pi e^2}{m_{\rm e}c}\,\lambda_0\, f\, n\, \Phi_v, \quad (13)$$

where λ_0 is the rest wavelength, f the absorption oscillator strength of the transition, and Φ_v the local absorption profile, given by

$$\Phi_v \;=\; \frac{1}{(2\pi)^{1/2}v_{\rm th}}\exp\left[-\frac{1}{2}\left(\frac{v-v_{\rm D}}{v_{\rm th}}\right)^2\right]. \quad (14)$$

Here, $v_{\rm th}$ is the thermal velocity of hydrogen and $v_{\rm D}$ is the line-of-sight velocity. In the present model, $v_{\rm D}$ is given by

$$\begin{aligned} v_{\rm D} \;=\; & \{u_r(r)\sin(\omega t-\phi)\cos\phi \\ & +[r\Omega(r)+u_\phi(r)\cos(\omega t-\phi)]\sin\phi\}\,\sin i \\ & +\frac{3z}{2r}u_r\sin(\omega t-\phi)\cos i, \end{aligned} \quad (15)$$

where i is the inclination angle between the observer's line-of-sight and the direction normal to the equatorial plane. Since the disk is geometrically thin, the last term on the right-hand side in equation (15), i.e., the line-of-sight component of the vertical velocity perturbation, is negligible unless $i \sim 0°$.

Figure 2 shows the $v_{\rm D}$ and $n(r,\phi,0)$ distributions for $r_{\rm out}/r_{\rm s} = 10$. Figure 2a is for $\alpha = 2$ and figure 2b for $\alpha = 3$. The value of $v_{\rm D}$ is calculated for $i = 90°$. The observer is in the downward direction on the figure. The phase of the variations is 0.25. (We choose phase 0 to be the phase at which the peak of ρ_1/ρ_0 locates in front of the star. Hence, the profile asymmetry is largest at phases 0.25 and 0.75.) In each figure the innermost circle and the outermost oval denote the location of the star/disk interface and the disk outer radius, respectively. The distribution of the equatorial population density $n(r,\phi,0)$ is indicated by the logarithmic grayscale, and the line-of-sight velocity $v_{\rm D}$ is shown by contours. The solid and dashed contour levels start at $v_{\rm D} = 0\,{\rm km\,s^{-1}}$ and at $v_{\rm D} = -50\,{\rm km\,s^{-1}}$, respectively. The contours are separated by $50\,{\rm km\,s^{-1}}$.

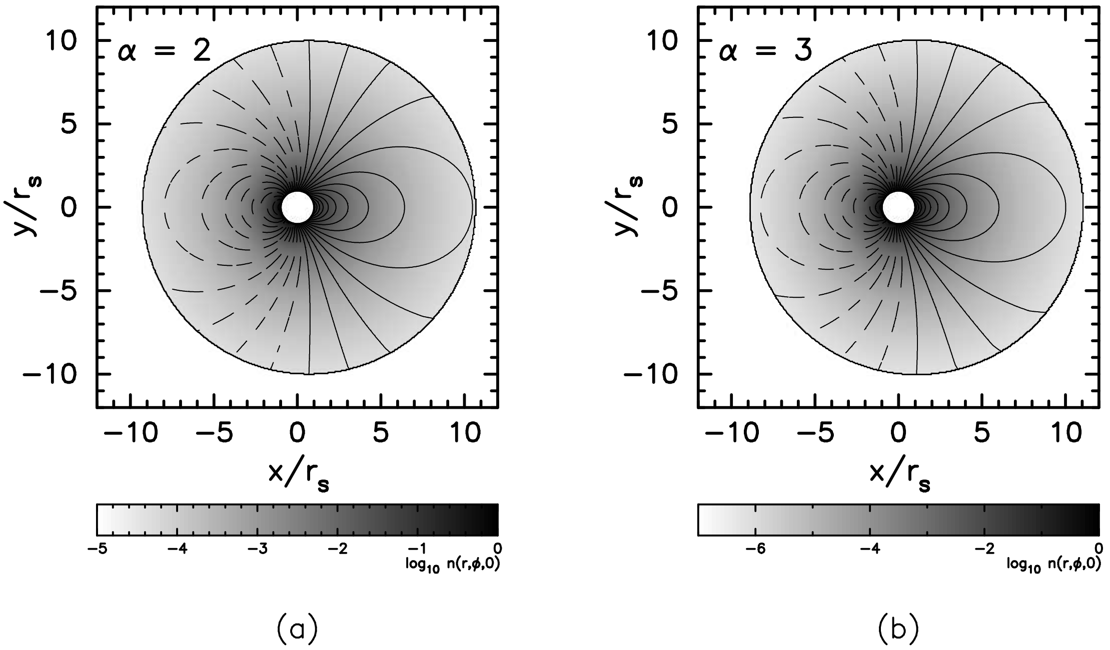

Fig. 2. Equatorial-plane distributions of the line-of-sight velocity $v_{\rm D}$ for $i=90^\circ$ and the population density $n(r,\phi,0)$ for (a) $\alpha=2$ and (b) $\alpha=3$. The observer is in the downward direction. The pahse is at 0.25. In each figure the innermost circle and the outermost oval denote the location of the star/disk interface and the disk outer radius, respectively. The equatorial population density is shown by the logarithmic grayscale and the line-of-sight velocity is shown by contours. The solid and dashed contour levels start at $v_{\rm D}=0{\rm km\,s^{-1}}$ and at $v_{\rm D}=-50{\rm km\,s^{-1}}$, respectively. The contours are separated by $50\,{\rm km\,s^{-1}}$.

In figure 2 we notice that the perturbed disk becomes eccentric due to the fundamental $m=1$ mode, and that, except for the innermost part of the disk, the velocity field associated with the perturbation points toward the observer. These features imply that optically-thick line profiles from disks perturbed by the one-armed fundamental modes vary in a manner in which the profile as a whole shifts blueward (redward) when the red (violet) peak is stronger.

The optical depths of the lines are often used to discuss the profiles. Hence, in order to characterize the population density of the unperturbed disk, we introduce the characteristic optical depth τ_0 defined by

$$\begin{aligned}\tau_0 &= \frac{\pi^{1/2}e^2\lambda_0 f}{2^{1/2}m_{\rm e}cv_{\rm th}}\int_{-\infty}^{\infty} n_0(r_{\rm s},z)\,dz \\ &= \frac{\pi e^2\lambda_0 f}{2^{1/2}m_{\rm e}cv_{\rm th}}\,H(r_{\rm s})n(r_{\rm s},0). \end{aligned}\tag{16}$$

We can then express the absorption coefficient κ_v as

$$\begin{aligned}\kappa_v &= \frac{\tau_0}{\pi^{1/2}H(r_{\rm s})}\left[1+\frac{\rho_{10}(r)}{\rho_{00}(r)}\cos(\omega t-\phi)\right]^2 \\ &\quad\times\left(\frac{r}{r_{\rm s}}\right)^{-2\alpha}\exp\left(-\frac{z^2}{H^2}\right) \\ &\quad\times\exp\left[-\frac{1}{2}\left(\frac{v-v_{\rm D}}{v_{\rm th}}\right)^2\right]. \end{aligned}\tag{17}$$

We compute the emission line profiles by integrating the surface intensities along $O(10^4)$ parallel rays penetrating the disk under the inclination angle i. The rays are more concentrated towards the higher-density, more rapidly rotating region around the star. For simplicity, we assume that the source function $S_{\rm L}$ is constant over the entire disk region. Then, the surface intensity I_v along each ray is simply reduced to

$$I_v = S_{\rm L}\left[1-\exp(-\tau_v)\right], \tag{18}$$

where the optical depth along the ray τ_v is given by

$$\tau_v = \int \kappa_v\,ds. \tag{19}$$

Here, ds is the line element along the ray. We evaluated the line integral in equation (19) using the values of κ_v on the $O(10^2)$ depth steps along the ray. In these calculations we adopted a somewhat crude velocity resolution of $10\,{\rm km\,s^{-1}}$ in order to reduce the computing time.

In subsequent sections we also present profiles of optically-thin emission lines for the sake of a comparison

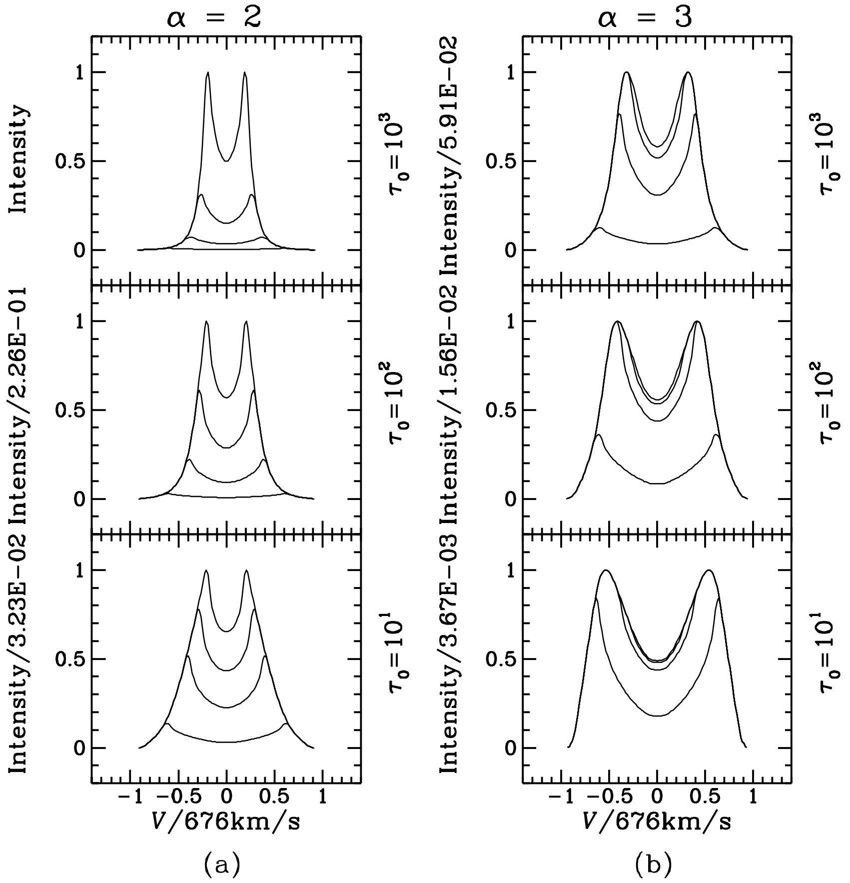

Fig. 3. Line profiles from the unperturbed disks for (a) $\alpha = 2$ and (b) $\alpha = 3$. The panels are for $\tau_0 = 10^3$, 10^2, and 10 from top to bottom, respectively. The four profiles in each panel are for $r_{\rm out}/r_s = 2$, 5, 10, and 20. Each profile is normalized by the peak intensity of the profile for $\alpha = 2$, $r_{\rm out}/r_s = 20$, and $\tau_0 = 10^3$.

with optically-thick line profiles. To obtain the optically-thin profiles, we adopted a method slightly different from that described above. The method using a bundle of rays is not adequate for calculating the optically-thin lines. It needs too many rays, each of which must have a large number of depth steps for computing the optically-thin line profiles with a sufficient accuracy. Hence, instead of calculating the surface intensities along rays, we integrated the line absorption coefficient κ_v given by equation (13) over the entire volume of the disk, because I_v in equation (18) is approximated to be proportional to τ_v for the optically-thin lines.

4. Emission-Line Profiles from the Unperturbed Disks

In this and subsequent sections we present the numerical results obtained by the method described in the previous section. We computed line profiles for disk sizes of $r_{\rm out}/r_{\rm s} = 5$, 10, and 20, density-gradient indices of $\alpha = 1$, 2, 3, and 4, characteristic optical depths of $\tau_0 = 10^3$, 10^2, and 10 and an optically thin case, and inclination angles of $i = 30°$, $60°$, and $90°$. Note that observed Hα emission arises, on the average, in the $7 - 19\, r_{\rm s}$ range (Slettebak et al. 1992).

Here, we comment on the range of τ_0 estimated for the disks of actual Be stars. For shell ($i = 90°$) stars, the optical depths of the envelopes are determined by the central depth analysis of the observed shell absorption lines (e.g., Kogure et al. 1978). Kogure (1990) collected the results obtained for some shell stars, and concluded that the optical depths in Hα lines τ_α range from 2000 to 5000 for fully-developed shell stars, while $\tau_\alpha \leq 100$ for weak shell stars. On the other hand, we can estimate τ_α for $i = 90°$ in our model as

$$\tau_\alpha \sim \int_{r_{\rm s}}^{r_{\rm out}} \kappa_{v=0}\, dr \sim \tau_0 \frac{r_{\rm s}}{\sqrt{2\pi} H(r_{\rm s})} \sim 10\, \tau_0. \qquad (20)$$

Hence, we found that disks of the actual Be stars are characterized by $10 \lesssim \tau_0 < 10^3$.

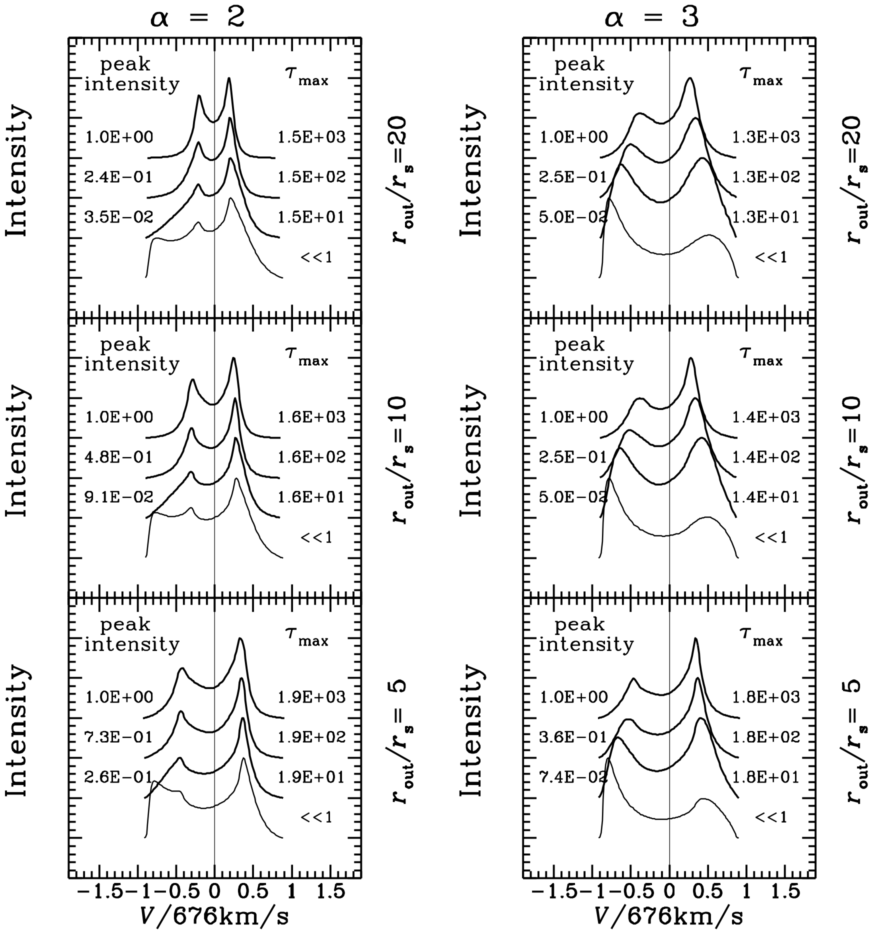

(a) (b)

Fig. 4. Line profiles from disks with $m = 1$ perturbation patterns at a phase of 0.25. The left panels are for $\alpha = 2$ and the right panels for $\alpha = 3$. The inclination angle of the disk is 60°. The panels, from top to bottom, are for $r_{\rm out}/r_{\rm s} = 20$, 10, and 5, respectively. Four profiles in each panel are for $\tau_0 = 10^3$, 10^2, 10, and $\tau_0 \ll 1$ from top to bottom, respectively. On both sides of each profile, the higher-peak intensity normalized by the peak intensity of the unperturbed profile for $\tau_0 = 10^3$ and the maximum optical depth are given.

Figure 3 shows the various line profiles from the unperturbed disks for $i = 60°$. The left panels are for $\alpha = 2$ and the right panels for $\alpha = 3$. The panels are for $\tau_0 = 10^3$, 10^2, and 10 from top to bottom, respectively. In each panel we show profiles for four outer disk radii: $r_{\rm out}/r_{\rm s} = 2$, 5, 10, and 20. Each profile is normalized by the peak intensity of the unperturbed profile from the disk with $\alpha = 2$, $r_{\rm out}/r_{\rm s} = 20$, and $\tau_0 = 10^3$. Except for the line widths, the profiles for $i = 30°$ and $i = 90°$ are roughly the same as those shown in figure 3.

We now consider the effects of the density gradient index α and the optical depth τ_0 on the line profiles. As demonstrated by Horne and Marsh (1986), the intensities along the line-of-sights through the high-density region saturate in optically-thick cases. Hence, the area under the saturated line intensity increases with increasing characteristic optical depth τ_0. Simultaneously, the unsaturated intensities from an outer region of the disk increases with τ_0. As a result, the contribution of the outer region of the disk monotonically increases with τ_0.

On the other hand, the velocities of the violet and red peaks for $\alpha = 2$ are independent of τ_0, and are given by $\pm(GM/r_{\rm out})^{1/2}$, while those for $\alpha = 3$ decrease towards $\pm(GM/r_{\rm out})^{1/2}$ as τ_0 increases. This feature can be understood as follows: The emission in each velocity bin arises from a different crescent-shaped region of the disk surface [see figure 2 and also figure 1 of Horne and Marsh (1986)]. For $\alpha \lesssim 2$, the strongest emission arises, irrespective of τ_0, from the crescent-shaped region tangent to the outer radius of the disk. For $\alpha \gtrsim 3$, however, it arises from the crescent-shaped region tangent to the radius where the optical depths along the line-of-sights

Table 1. The amplitude of V/R variations.

α	τ_0		$r_{\rm out}/r_s=5$			$r_{\rm out}/r_s=10$			$r_{\rm out}/r_s=20$		
			30°	60°	90°	30°	60°	90°	30°	60°	90°
1	10^3	$({\rm V/R})_{\rm max}$ ...	1.4	1.4	1.4	1.2	1.2	1.2	1.1	1.1	1.0
		Δv_r	15	20	30	5	5	10	0	0	0
	10^2	$({\rm V/R})_{\rm max}$ ...	1.4	1.4	1.4	1.2	1.2	1.2	1.1	1.1	1.0
		Δv_r	15	20	25	5	5	10	0	0	0
	10	$({\rm V/R})_{\rm max}$ ...	1.5	1.5	1.4	1.2	1.2	1.2	1.1	1.1	1.1
		Δv_r	10	20	30	5	10	10	0	5	0
2	10^3	$({\rm V/R})_{\rm max}$ ...	1.6	1.6	1.5	1.4	1.4	1.3	1.3	1.3	1.2
		Δv_r	20	30	35	10	15	15	5	5	10
	10^2	$({\rm V/R})_{\rm max}$ ...	1.7	1.7	1.6	1.6	1.6	1.5	1.4	1.4	1.4
		Δv_r	15	35	35	10	10	15	0	5	5
	10	$({\rm V/R})_{\rm max}$ ...	1.8	2.0	1.9	1.6	1.7	1.8	1.4	1.5	1.6
		Δv_r	20	35	35	5	15	15	0	0	5
3	10^3	$({\rm V/R})_{\rm max}$ ...	1.9	2.0	1.8	1.9	2.0	2.1	1.7	1.8	1.9
		Δv_r	25	40	45	20	35	30	25	40	40
	10^2	$({\rm V/R})_{\rm max}$ ...	1.8	2.1	2.1	1.5	1.7	1.9	1.4	1.5	1.7
		Δv_r	35	55	45	35	60	60	30	55	55
	10	$({\rm V/R})_{\rm max}$ ...	1.2	1.3	1.7	1.0	1.1	1.4	1.0	1.1	1.3
		Δv_r	55	85	85	45	80	75	40	70	65
4	10^3	$({\rm V/R})_{\rm max}$ ...	1.6	1.8	2.1	1.2	1.3	1.5	1.1	1.1	1.2
		Δv_r	40	60	65	25	45	50	15	25	30
	10^2	$({\rm V/R})_{\rm max}$ ...	1.1	1.3	1.6	1.0	1.1	1.3	1.0	1.0	1.1
		Δv_r	30	60	65	20	35	45	−10	25	25
	10	$({\rm V/R})_{\rm max}$ ...	1.2	1.2	1.1	1.2	1.1	1.0	1.1	1.1	1.0
		Δv_r	−25	−45	55	−10	−25	30	−10	−20	−15

are almost unity. This radius increases with increasing τ_0. Thus, for $\alpha \gtrsim 3$, the peak velocity is a measure for a radius within which most of the emission arises.

5. Variations of Line Profiles Due to $m = 1$ Perturbation Patterns

We now consider the variabilities in the line profiles from disks with $m = 1$ perturbation patterns. Our interests are in whether the line profiles exhibit variabilities similar to the observed V/R variations, and how the variabilities depend on the adopted perturbation patterns.

Figure 4 shows the line profiles at a phase of 0.25 for different values of α, $r_{\rm out}/r_{\rm s}$, and τ_0. Recall that the profile asymmetry is largest at phases of 0.25 and 0.75. The inclination angle of the disk is 60°. The left panels are for $\alpha = 2$ and the right panels for $\alpha = 3$. The panels, from top to bottom, are for $r_{\rm out}/r_{\rm s} = 20$, 10, and 5, respectively. In each panel four profiles are shown for different values of the characteristic optical depth τ_0. They are for $\tau_0 = 10^3$, 10^2, 10, and $\tau_0 \ll 1$ from top to bottom, respectively. On both sides of each profile, we give the intensity of the higher peak normalized so that the peak intensity of the unperturbed profile for $\tau_0 = 10^3$ is unity and the maximum optical depth $\tau_{\rm max}$. Here, $\tau_{\rm max}$ is defined by the maximum value among the optical depths along rays through the entire disk, and is regarded as an approximation to τ_α.

Note that the line profiles exhibit remarkable V/R asymmetries for a wide range of disk parameters. Furthermore, note that the line center velocity of each optically-thick profile is negative; in other words, the profile as a whole shifts in the direction of the weaker emission component. Thus, the line-profile variabilities from disks with $m = 1$ perturbation patterns are in agreement with the global characteristics of the observed V/R variations.

To study the model line profiles in more detail, we give in table 1 two quantities which characterize the behavior of the line-profile variation. One is the maximum value of the V/R ratio $({\rm V/R})_{\rm max}$, which is defined by the ratio of the violet and red peak intensities. The other is the radial-velocity displacement Δv_r defined by the mean of the violet and red peak velocities at the phase of the maximum V/R ratio. Recall that $\Delta v_r > 0$ for the observed V/R variations of the Balmer lines.

Let us consider the characteristics of the line-profile variabilities caused by $m = 1$ perturbation patterns. First, we note from table 1 that $\Delta v_r > 0$ for a wide range of disk parameters. This means that (in general terms) the one-armed oscillation scenario agrees well with the observed V/R variations. Note that this result is insensitive to the details of the model. Second, we also note that the value of Δv_r is sensitive to the detailed form of the perturbation patterns adopted. In the present model, for $\alpha = 2$, the V/R ratio varies with a large amplitude, while no significant profile-shift occurs. In contrast, the disks with $\alpha = 3$ exhibit large-amplitude V/R variations similar to the observed variations for a wide range of disk sizes and optical depths. This difference in the profile

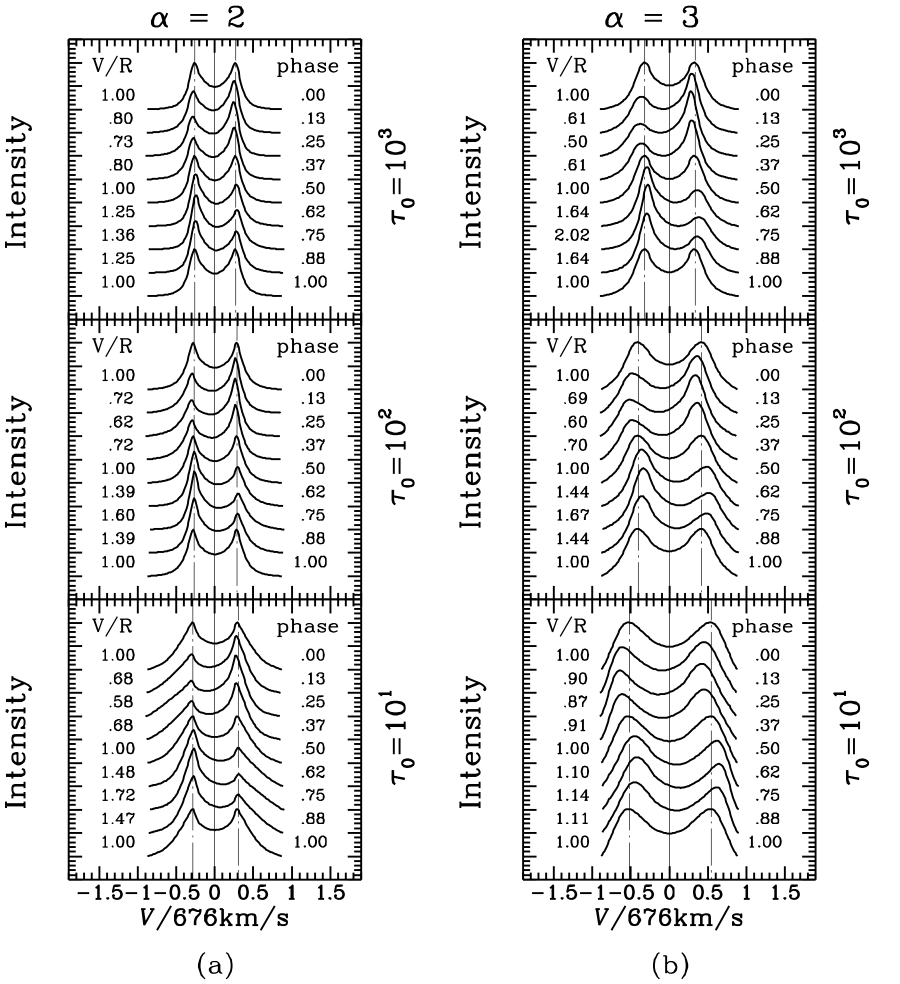

Fig. 5. Line-profile variabilities due to $m = 1$ perturbation patterns for (a) $\alpha = 2$ and (b) $\alpha = 3$. The profiles are for $r_{\rm out}/r_s = 10$ and $i = 60°$. The panels correspond to $\tau_0 = 10^3$, 10^2, and 10 from top to bottom, respectively. In each panel the line profile variability is shown by the profiles at the eight different phases. On both sides of each profile, the V/R ratio and the phase are given. The vertical dash-dotted lines denote the peak velocities of the unperturbed profiles.

variabilities arises from the difference in the perturbed disk structures for $\alpha = 2$ and $\alpha = 3$. Recall that for $\alpha = 2$, the peak velocity is equal to the velocity at the disk outer radius, while for $\alpha = 3$ it is equal to the velocity at the radius within which the disk is optically thick for the line. For $r_{\rm out}/r_{\rm s} \geq 10$ and $i = 60°$, the latter radius is about 3, 4, and 7 for $\tau_0 = 10$, 10^2, and 10^3, respectively. In our model, the amplitude of the perturbation at the disk outer radius for $\alpha = 2$ is much smaller than that at the radius with the optical depth about unity for $\alpha = 3$. As a result, the profile shift for $\alpha = 2$ is much smaller than that for $\alpha = 3$. The reason why the amplitude of the V/R variation for $r_{\rm out}/r_{\rm s} = 5$ is large irrespective of α is that the amplitude of the perturbation is large even at the disk outer radius. Note that, in principle, the disk-structure dependent feature of the line-profile variabilities can be used to probe the disk structure of Be stars, although the present model is too simple to enable us to extract any detailed information concerning the disk structure from the observed variabilities.

To illustrate the behavior of the profile variations more explicitly, we present some examples of the V/R variations in figure 5. In this figure, $r_{\rm out}/r_{\rm s} = 10$ and the inclination angle i is 60°. Figure 5 shows the line-profile variabilities due to the fundamental modes for $\alpha = 2$ (left) and $\alpha = 3$ (right). The oscillation periods of the modes are -30.2 yr for $\alpha = 2$ and -10.6 yr for $\alpha = 3$. The panels correspond to $\tau_0 = 10^3$, 10^2, and 10 from top to bottom, respectively. In each panel the line-profile variability is shown by the profiles at eight different phases. The vertical dash-dotted lines denote the peak velocities of the unperturbed profiles. For $\alpha = 2$, the peak velocities show little time variabilities, although the V/R ratios vary significantly. In contrast, for $\alpha = 3$, the peak velocities as well as the V/R ratios exhibit remarkable variations when $\tau_0 \geq 10^2$. Note that the range of τ_0 for these remarkable variations roughly covers the observed range of Hα-line optical depth.

In summary, line profiles from the disks perturbed by the $m = 1$ perturbation patterns exhibit long-term V/R variations similar to the observed variations of the Balmer lines. These V/R variations occur for a wide range of disk sizes ($r_{\rm out}/r_{\rm s} \gtrsim 5$) and optical depths ($\tau_{\rm max} \gtrsim 10^2$). In the present model, the amplitude of the V/R variation is larger for disks with steep ($\alpha \gtrsim 3$) density gradients than for disks with flat ($\alpha \lesssim 2$) density gradients.

6. Summary

In Paper I we proposed a model for the long-term V/R variations of Be stars. Examining the linear, one-armed, isothermal oscillations in isothermal equatorial disks, we found that this model well reproduces the periodicity of the observed long-term V/R variations for a range of disk sizes $r_{\rm out}/r_{\rm s}$ and density-gradient indices α.

In this paper we have considered the profile variabilities of Balmer lines caused by the one-armed isothermal oscillations studied in Paper I. In order to examine the effects of one-armed oscillations on line profiles, we assumed nonlinear perturbation patterns similar to the linear $m = 1$ eigenfunctions. The eigenfunctions were normalized so that the maximum value of the perturbed part of the angular velocity u_ϕ is 10 % of the unperturbed part $r\Omega$. In addition, we assumed that the source function is constant over the entire disk region. Based on these assumptions, we studied the profile variations by computing fluxes along a bundle of line-of-sights for various values of disk sizes $r_{\rm out}/r_{\rm s}$, density gradient indices α, characteristic optical depths τ_0, and inclination angles i. We took only the thermal broadening into account as the line-broadening mechanism. As a result of this study, the following conclusions have been derived:

1. For a line profile from a disk with a density distribution of $\alpha \lesssim 2$, the peak separation is given by $2\,(GM/r_{\rm out})^{1/2}$, and is independent of the line optical depth. This is because the largest contribution to the total emission for $\alpha \lesssim 2$ arises from the constant line-of-sight velocity region tangent to the disk outer radius. On the other hand, for a steeper ($\alpha \gtrsim 3$) density distribution, the largest contribution arises from the constant line-of-sight velocity region tangent to the radius where the optical depths along the line-of-sights are about unity. Thus, for $\alpha \gtrsim 3$, the peak separation decreases towards $2\,(GM/r_{\rm out})^{1/2}$ along with an increase in the line optical depth.

2. For a wide range of disk parameters, the line profiles from disks with $m = 1$ perturbation patterns exhibit remarkable V/R asymmetries. The profile as a whole shifts redward (blueward) when V/R > 1 (V/R < 1). These features are insensitive to the detailed disk structure adopted. We thus conclude that in general terms the one-armed oscillation scenario agrees well with the observed V/R variability. On the other hand, the amplitude of the profile shift associated with the V/R variation is sensitive to the perturbed disk structure. In the present model it is larger for disks with steep ($\alpha \gtrsim 3$) density gradients than for disks with flat ($\alpha \lesssim 2$) density gradients. This is because the amplitude of the perturbation is larger for $\alpha = 3$ than for $\alpha = 2$ at the region from which the largest contribution to the total emission arises. In principle, this disk-structure dependent feature can be used to probe the structure of Be-star disks.

In this paper we assumed perturbation patterns similar to the linear eigenfunctions and the constant-source function to study the effects of the one-armed oscillations on line profiles. Consideration of the effect of the nonuniform source function is expected to provide only minor modifications to the above conclusions. Taking the nonlinear effects exactly into account, however, can modify the results obtained in this paper, since the amplitude of the V/R variation depends on the detailed forms of the eigenfunctions. In addition, the periods and eigenfunctions are sensitive to the disk models adopted. Therefore, it is highly desired to investigate the nonlinear one-armed modes in equatorial disks of Be stars.

It is a pleasure to thank R. Hirata, S. Kato, M. Mon, and T. Horaguchi for stimulating discussions. The hospitalities of the Department of Astronomy, Kyoto University and Astronomical Institute, University of Amsterdam are also greatly appreciated. The author wishes to acknowledge financial support of the Foundation for Inservice Trading and Welfare of the Private School Personnel. This work was partially supported by a grant from the Hokkai-Gakuen Educational Foundation.

References

Adam J., Innes D. E., Shaviv G., Störzer H., Wehrse R. 1989a, in Theory of Accretion Disks, ed F. Meyer, W. J. Duschl, J. Frank, E. Meyer-Hofmeister (Kluwer Academic Publishers, Dordrecht) p403

Adam J., Störzer H., Duschl W. J. 1989b, A&A 218, 205

Adams F. C., Ruden S. P., Shu F. H. 1989, ApJ 347, 959

Allen C.W. 1973, Astrophysical Quantities, 3rd ed (The Athlone Press, London) pp206, 209

Ballereau D., Chauville J. 1989, A&A 214, 285

Claret A., Giménez A. 1991, A&AS 87, 507

Copeland J. A., Heard J. F. 1963, Publ. David Dunlap Obs. 2, 317

Hanuschik R. W., Hummel W., Dietle O., Sutorius E. 1995, A&A 300, 163
Hirata R., Hubert-Delplace A. -M. 1981, in Workshop on Pulsating B Stars, ed M. Auvergne, A. Baglin, D. Ducatel, J. -M. Le Contel, P. J. Morel, J. -P. Sareyan, J. -C. Valtier, C. Sterken (Observatoire de Nice, Nice) p217
Hirata R., Kogure T. 1984, Bull. Astron. Soc. India 12, 109
Horne K., Marsh T.R. 1986, MNRAS 218, 761
Huang S.-S. 1975, Sky and Telescope 49, 359
Hubert A.M., Floquet M., Chambon M.T. 1987, A&A 186, 213
Hummel W., Hanuschik R.W. 1994, in Pulsation, Rotation, and Mass Loss of Early Type Stars, IAU Symp. No.162, ed L.A. Balona, H.F. Henrichs, J.M. Le Contel (Kluwer Academic Publisher, Dordrecht) p382
Kato S. 1983, PASJ 35, 249
Kato S. 1989, in Theory of Accretion Disks, ed F. Meyer, W. J. Duschl, J. Frank, E. Meyer-Hofmeister (Kluwer Academic Publishers, Dordrecht) p173
Kogure T. 1990, Ap&SS 163, 7
Kogure T., Hirata R. 1982, Bull. Astron. Soc. India 10, 281
Kogure T., Hirata R., Asada Y. 1978, PASJ 30, 385
Marlborough J. M. 1969, ApJ 156, 135
Marlborough J. M. 1970, ApJ 159, 575
McLaughlin D. B. 1961, J. Roy. Astron. Soc. Canada 55, 73
McLaughlin D. B. 1962, ApJS 7, 65
McLaughlin D. B. 1963, ApJ 137, 1085
McLaughlin D. B. 1966, ApJ 143, 285
Okazaki A. T. 1991, PASJ 43, 75 (Paper I)
Okazaki A. T., Kato S. 1985, PASJ 37, 683
Papaloizou J. C., Savonije G. J., Henrichs H. F. 1992, A&A 265, L45
Poeckert R. 1982, in Be stars, IAU Symp. No.98, ed M. Jaschek, H. -G. Groth (D. Reidel Publishing Company, Dordrecht), p453
Poeckert R., Marlborough J. M. 1978, ApJ 220, 940
Savonije G. J., Heemskerk M. H. M. 1993, A&A 276, 409
Slettebak A. 1982, ApJS 50, 55
Slettebak A., Collins G. W. II, Truax R. 1992, ApJS 81, 335